

Phonon Topology on the Time-Reversal Symmetric Honeycomb

Juan L. Mañes¹

¹*Departamento de Física de la Materia Condensada, Universidad del País Vasco UPV/EHU*
(Dated: September 4, 2022)

We use the methods of Topological Quantum Chemistry to explore the topology of phonons on time-reversal symmetric crystals with the structure of the planar honeycomb. This approach is not tied to a particular model of atomic vibrations, but is applied to the most general dynamical matrix constrained only by the symmetries of the system. We show that four distinct topological phases are generically possible. Truncating the dynamical matrix to third nearest neighbors yields a model that realizes the different phonon topologies, characterized by the existence of phononic edge and corner modes and by Wilson loops with winding numbers one and two. Fitting the dynamical matrix to the DFT phonon bands shows that graphene is not very far from a topologically nontrivial phase.

Introduction The honeycomb lattice has played an important role in our understanding of topological states of matter. The Haldane [1] and Kane-Mele [2, 3] models have clarified the effects of time-reversal symmetry, or its absence, on the topology of electron hamiltonians. For phonons, rotating honeycomb lattices [4–6] where the Coriolis force plays the role of a magnetic field and gyroscopic phononic crystals [7] have been used to study the existence of nontrivial phonon topology in the absence of time-reversal symmetry. More recently, topological phonons have been reported on the valley-mixing Kekulé deformation of the honeycomb lattice [8].

The methods of Topological Quantum Chemistry (TQC) [9], which provide a reliable and systematic way to predict all the topologically nontrivial phases consistent with a given crystal structure, have been used to uncover thousands of new materials with nontrivial electron band topology [10]. But the methods of TQC have not, to the best of our knowledge, been applied to the search for nontrivial topology in phonon spectra. In this letter we adapt the methods of TQC to the analysis of phonon bands, and use them to unveil the existence of four previously unknown topological phases on the time-reversal symmetric planar honeycomb. These phases are characterized by the existence of edge and corner phonon modes and nontrivial windings in the Wilson line spectra.

atomic orbitals in a crystal transform under the symmetry operations of the space group of the crystal. As the number of atoms in an ideal crystal is infinite, a band representation is an infinite dimensional representation of the space group. The Bloch-wave combinations $\sum_{\mathbf{R}} \exp(i\mathbf{k} \cdot \mathbf{R}) \phi_i(\mathbf{r} - \mathbf{R})$ of atomic orbitals [14] transform according to a representation of the little group $G_{\mathbf{k}}$ [15]. Thus a band representation induces little group representations at all the points in the Brillouin zone (BZ).

A band representation that can not be written as the sum of two band representations is an elementary band representation (EBR). With some exceptions that are well understood and tabulated [13, 16], an EBR is generated from a set of orbitals that transform under an irreducible representation (irrep) D of the local site symmetry group G_w of a maximal symmetry Wyckoff position (WP) w . The corresponding EBR is denoted by $D \uparrow G|_w$.

Any band representation is either elementary or can be written as a sum of EBRs. If a subset of bands is separated by a gap from the other bands and does not transform as a band representation, then the subset does not have an atomic limit and is topologically nontrivial [9]. This gives an efficient method to identify topologically nontrivial subsets of bands. In practical terms, one considers the irreps describing the transformation of the subset of bands at the high symmetry points in the Brillouin zone. If the collection of little group irreps can not be obtained from a sum of EBRs, then the subset of bands has nontrivial topology. This method will be applied below to the phonon bands of the honeycomb.

Band representations for phonons The concept of band representation is easily extended to the atomic vibrations of a crystal [17]. Instead of atomic orbitals, one considers the set of vectors giving the displacements from equilibrium of all the atoms in the crystal and their transformation properties. This defines the “mechanical” band representation. Intuitively, the mechanical band representation can be understood as an electron band representation with (spinless) p -orbitals, since p -orbitals, like atomic displacements, transform according to the “vector” representation V [15]. Thus the mechanical

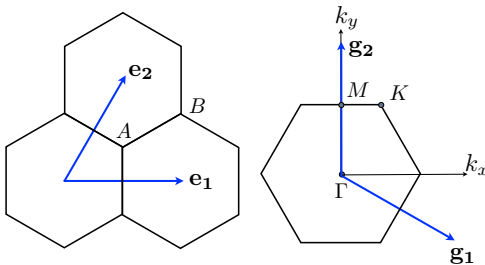


FIG. 1. Direct and reciprocal lattice basis vectors

Elementary band representations and band topology One key concept in the TQC framework is that of (elementary) band representations [11–13]. Roughly speaking, a band representation describes how the set of

band representation M is induced from the vector representation at each occupied Wyckoff position w in the crystal i.e., $M = \sum_w V \uparrow G|_w$.

An important difference between electron and phonon band representations concerns the number of degrees of freedom and their location. Electronic orbitals are functions defined throughout space, and we can consider many orbitals in an atom, while an atomic displacement is described just by a single vector at the atom location. As a consequence, the number of phonon bands is equal to three times the number of atoms in the primitive unit cell. Another property of phonon bands without parallel in electrons is the existence of three acoustic bands, that must satisfy the constraint $\lim_{\mathbf{k} \rightarrow 0} \omega(\mathbf{k}) = 0$. The acoustic modes at $\mathbf{k} = 0$ represent uniform translations \mathbf{t} of all the atoms in the crystal and transform according to the vector representation V .

Mechanical band representation for the planar honeycomb The layer group for the planar honeycomb is LG 80, which corresponds to the space group SG 191 ($P6/mmm$). In-plane (x, y) and off-plane (z) vibrations of the lattice are respectively even and odd under reflections on the horizontal mirror plane, and decouple in the harmonic approximation. Thus, for practical purposes, it is sufficient and simpler to consider the subgroup SG 183 ($P6mm$), while treating in-plane and off-plane vibrations separately. The atoms in the honeycomb lattice are at the Wyckoff position $2b$, with site symmetry group isomorphic to the point group $3m$ (C_{3v}). The vector representation for $3m$ is reducible, $V = A_1(z) + E(x, y)$ [15]. This implies that the mechanical band representation can be written as the sum of two EBRs induced respectively from A_1 and E at $2b$, i.e., $M = A_1 \uparrow G|_{2b} + E \uparrow G|_{2b}$, that describe the transformation properties of the two off-plane and four in-plane bands.

The Bilbao Crystallographic Server (BCS) [18, 19] gives the irreps induced by any EBR at the high symmetry points in the BZ, and also tells whether the EBR is decomposable [20, 21]. An EBR is decomposable if the

corresponding band can be split into two sets separated by a gap. It is known that a split EBR always gives rise to a topologically nontrivial phase [9, 22]. According to the BCS, $M = A_1 \uparrow G|_{2b}$ is indecomposable [23]. On the other hand, $E \uparrow G|_{2b}$ is decomposable and, as a consequence, the four in-plane bands can split into two disconnected sets. Table I gives, for all the subsets consistent with the compatibility relations, the irreps at the three high symmetry points in the BZ. The acoustic branches are identified by noting that the vector representation at the Γ point is given by $V = \Gamma_1(z) + \Gamma_6(x, y)$ and therefore Γ_6 is associated with uniform in-plane translations.

The next step is to determine which of the branches in Table I can transform as band representations. To this end, we try to obtain sums of EBRs that induce the same little group irreps at the high symmetry points in the BZ. It turns out that this is possible only for the op-

Phase	Acoustic branch	Optical branch
Ia	$\Gamma_6; K_1 + K_2; M_1 + M_2$	$\Gamma_5; K_3; M_3 + M_4$
Ib	$\Gamma_6; K_3; M_1 + M_2$	$\Gamma_5; K_1 + K_2; M_3 + M_4$
IIa	$\Gamma_6; K_1 + K_2; M_3 + M_4$	$\Gamma_5; K_3; M_1 + M_2$
IIf	$\Gamma_6; K_3; M_3 + M_4$	$\Gamma_5; K_1 + K_2; M_1 + M_2$

TABLE I. Irreps at the three high symmetry points in the BZ. All irreps are 1-dimensional, except for Γ_5 , Γ_6 and K_3 , which are 2-dimensional.

tical branch of phase IIa and the acoustic branch of IIf. As shown in Table II, in order to obtain the irreps of the remaining branches we must subtract some EBRs. This means that only the optical branch of phase IIa and the acoustic branch of IIf may transform as band representations, whereas the remaining six branches must be topologically nontrivial. This is consistent with the general result that says that, when a set of bands transforming as an EBR splits, at least one of the resulting subsets of bands must have nontrivial topology [22, 24]. The occurrence of negative coefficients in Table II suggests that the corresponding phases are topologically fragile [22, 25]. See, however, the comments at the end of this Letter.

Phase	Acoustic branch	Optical branch
Ia	$A_1 \uparrow G _{1a} - A_1 \uparrow G _{2b} + B_2 \uparrow G _{3c}$	$A_1 \uparrow G _{3c} - A_1 \uparrow G _{1a}$
Ib	$B_1 \uparrow G _{3c} - B_2 \uparrow G _{1a}$	$B_1 \uparrow G _{1a} + E \uparrow G _{2b} - B_2 \uparrow G _{3c}$
IIa	$E \uparrow G _{2b} - E_2 \uparrow G _{1a}$	$E_2 \uparrow G _{1a}$
IIf	$E_1 \uparrow G _{1a}$	$E \uparrow G _{2b} - E_1 \uparrow G _{1a}$

TABLE II. Combinations of EBRs that reproduce the irreps at the high symmetry points for the eight branches in Table I. Note that these combinations are in general non-unique.

The different phases in Table I are associated with the ordering of the phonon frequencies at points K and M . For example, in order to obtain phase Ia, $\omega(K_1)$ and $\omega(K_2)$

must be lower than $\omega(K_3)$, and $\omega(M_1)$ and $\omega(M_2)$ must also be lower than $\omega(M_3)$ and $\omega(M_4)$. This must be so in order to avoid band crossings between the two subsets,

as such band crossings would cause the subsets to reconnect [20]. For that reason, whenever $\omega(K_3)$ is between $\omega(K_1)$ and $\omega(K_2)$, the four bands are interconnected and we are in a topologically trivial phase. The frequencies at different points in the BZ are obtained by diagonalizing the dynamical matrix [26].

Dynamical matrix for in-plane modes The harmonic potential energy can be written as $U = 1/2 \sum_{i,j} \mathbf{r}_i^t U_{ij} \mathbf{r}_j$, where i, j run over all the atoms [27] in the lattice, $\mathbf{r}_i = (x_i, y_i)$ is the displacement of atom i from equilibrium and $U_{ij} = U_{ji}^t$ is the matrix of force constants between atoms i and j . Assuming that the atoms i, j are n th-nearest neighbors, the 2×2 matrix U_{ij} is parametrized by four real coefficients (a_n, b_n, c_n, d_n) , often with a single set of coefficients for all n th-neighbor pairs. As explained in the Supplemental Material (SM), some of these coefficients may be forced to vanish by the symmetries of the lattice.

Fourier transforming U_{ij} yields the dynamical matrix, which is given in Eq. (S10) with up to third nearest neighbor interactions. As shown in the SM, in order to describe a topological phase the following two necessary conditions must be simultaneously satisfied

$$2\sqrt{3}|d_2| > |b_1 + b_3| \quad (1)$$

$$|a_1 - 3a_3| > \text{Max}\{2|b_1|, 4|b_2|\}. \quad (2)$$

If either condition fails to be satisfied, we will be in a topologically trivial phase where all four bands are interconnected. When both conditions are satisfied, the concrete phase is given by: Ia ($d_2 < 0, a_1 < 3a_3$), Ib ($d_2 > 0, a_1 < 3a_3$), IIa ($d_2 < 0, a_1 > 3a_3$), and IIb ($d_2 > 0, a_1 > 3a_3$). This implies that phases Ia and Ib can be modeled by a dynamical matrix including up to second nearest neighbors, whereas third nearest neighbor interactions are required to obtain phases IIa and IIb. Note that, unlike the hamiltonian $H(\mathbf{k})$ for electron bands, the dynamical matrix has to satisfy several stability conditions to prevent the existence of imaginary phonon frequencies. For instance, imposing $\omega^2(\Gamma) > 0$ requires $a_1 + a_3 < 0$.

Wilson loops and boundary states Winding in the Wilson loop (WL) spectrum for a subset of isolated bands is a topological invariant. A winding that can not be eliminated by any perturbation that respects the symmetries of the system and does not close a gap guarantees that the subset of bands has nontrivial topology. We will consider a \mathbf{g}_1 -directed Wilson loop [28–32] defined by

$$W(k_2) \equiv P e^{i \int_0^{2\pi} dk_1 A_1(k_1, k_2)}, \quad (3)$$

where P indicates that the integral is path-ordered and $A_1(\mathbf{k})_{ij} = i \langle u_i(\mathbf{k}) | \partial_{k_1} u_j(\mathbf{k}) \rangle$ is the non-abelian Berry potential built from the normal modes $u_i(\mathbf{k})$ of a subset of isolated bands. We take k_1 along \mathbf{g}_1 (see Fig. 1) and k_2 along \mathbf{g}_2 . The eigenvalues of $W(k_2)$ are of the form $e^{2\pi i x(k_2)}$, where $x(k_2)$ is the position of the center of a

hybrid Wannier function [33, 34] along \mathbf{e}_1 . As the base-point moves along the k_2 -axis from Γ to M and back to Γ , the Wannier centers move along the 1-dimensional unit cell, as shown in Fig. 2.

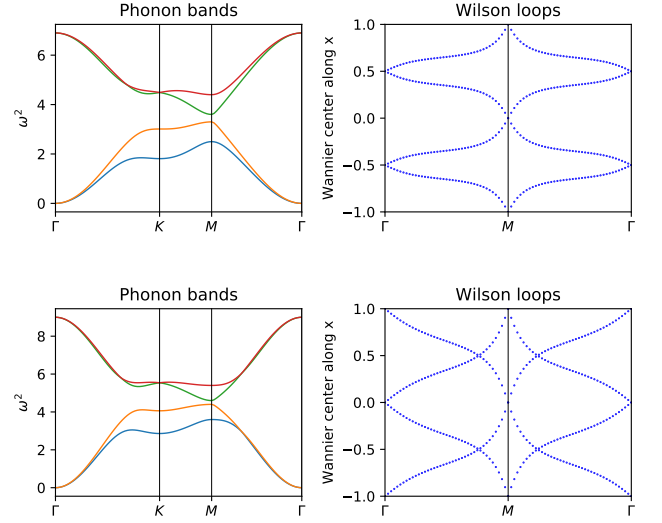


FIG. 2. Phonon bands (left) and Wannier centers for the acoustic bands (right). Top: $a_1 = -1, a_3 = -0.15, b_1 = -0.2, d_2 = 0.2, a_2 = b_2 = b_3 = 0$ (Phase Ib). Bottom: $a_1 = -1, a_3 = -0.5, b_1 = -0.2, d_2 = 0.2, a_2 = b_2 = b_3 = 0$ (Phase IIb)

According to Table II, all the branches but the optical one of phase IIa and the acoustic one of IIb are necessarily topological, as they do not transform as band representations. On the other hand, the irreps of the optical branch of phase IIa and the acoustic branch of IIb at the high symmetry points of the BZ are such that they *might* transform according to band representations and could be trivial. However, as shown in Fig. 2, the WL of the acoustic branch of IIb has winding number two, which implies that the branch has nontrivial topology. In fact, we find that the WLs of *all* eight branches in Table II have non-zero winding numbers, equal to one for phases Ia and Ib, and two for IIa and IIb. In other words, there are no trivial bands in the topological phases of this phonon system.

The windings of the WLs can be understood from the C_{2z} -eigenvalues of the normal modes at the two C_{2z} -invariant points, Γ and M . As shown in the SM, the eigenvalues are $+1$ for Γ_5, M_1 and M_2 , and -1 for Γ_6, M_3 and M_4 . Comparing with Table I, we see that the two bands in each branch of phases Ia and Ib have the same C_{2z} -eigenvalues at the Γ -point, and opposite to those at the M point. The converse is true for phases IIa and IIb, where the C_{2z} -eigenvalues at the Γ and M points are equal. Having opposite C_{2z} -eigenvalues at Γ and M forces the Wilson bands to wind, while having the same eigenvalues is compatible with zero or, more generally, even winding numbers [35]. In this case we can have a non-zero winding number because the crossings

at generic k_2 and Wannier center $x = \pm 1/2$ in Fig. 2 are protected by $C_{2z}\mathcal{T}$ invariance [24, 36], where \mathcal{T} is the time-reversal operation.

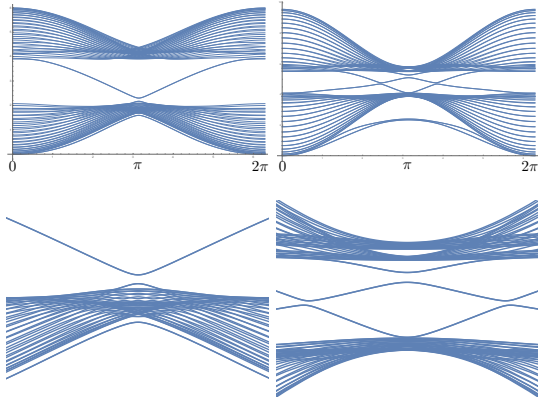


FIG. 3. Phonon edge modes. Top left: $a_1 = -1$, $b_1 = 0.05$, $d_2 = 0.2$, $a_2 = a_3 = b_2 = b_3 = 0$ (Phase Ib). Top right: $a_1 = -1$, $a_3 = -0.6$, $b_1 = 0.05$, $d_2 = 0.2$, $a_2 = b_2 = b_3 = 0$ (Phase Iib). Bottom: close-ups of the gaps.

Edge and corner modes In order to compute the edge modes we have imposed periodic boundary conditions in the x -direction (along \mathbf{e}_1 in Fig 1) and open boundary conditions on the two zig-zag edges. The results are presented in Fig 3, where k_x goes from 0 to 2π . The edge mode spectrum in phase Ib (Iib) is qualitatively identical to the spectrum in phase Ia (IIa). The edge modes present several peculiarities. First of all, besides the usual gap-crossing ‘optical’ edge modes, there are also ‘acoustic’ edge modes below the bulk acoustic branch. Secondly, the edge mode spectrum is gapped, as shown in the close-ups in Fig 3. This is typical of topologically fragile phases [25], and is consistent with the negative coefficients in the linear combinations of EBRs in Table II. Notice also that the edge mode spectrum is more complicated in the IIa and Iib phases, possibly reflecting the winding number two in the Wilson line spectrum. Lastly, there are also corner modes, as shown in Fig 4. This is again to be expected in topologically fragile phases, and is considered a signature of higher order topology [37, 38].

The corner modes in Fig 4 have been computed for a parallelogram cut along the unit vectors in Fig 1, with 40 unit cells per side and open boundary conditions along the resulting zig-zag edges. The corner modes appear at the 60 degree angles. For different values of the parameters we have also observed additional corner modes at the 120 degree angles, sometimes buried in the continuum spectrum. The slow damping rate of the corner modes along the edges is a reflection of the smallness of the gap in the edge mode spectrum.

Material realization The four in-plane phonon bands in graphene are interconnected and the spectrum is topologically trivial. However, fitting the DFT spectrum to

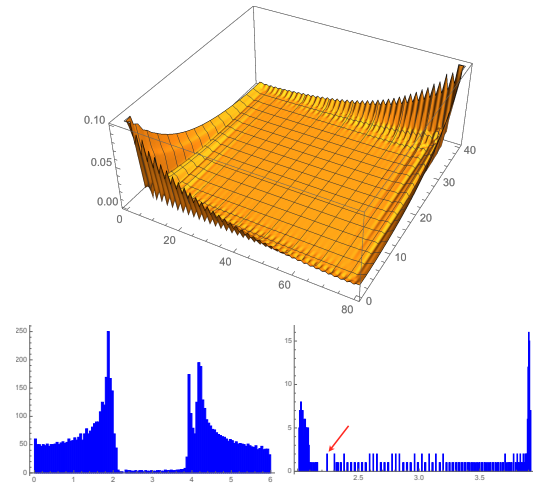


FIG. 4. Phononic corner modes for $a_1 = -1$, $b_1 = 0.05$, $d_2 = 0.2$, $a_2 = a_3 = b_2 = b_3 = 0$ (Phase Ib). Top: Oscillation amplitudes for the corner modes. Bottom left: Phonon DOS. Bottom right: DOS of the bulk gap, with arrowed degenerate corner modes.

our third nearest neighbor dynamical matrix shows that graphene is not too far from having a topologically non-trivial phonon spectrum. Concretely, we show in the SM that topological Phase Ia can be reached by changing the values of b_1 , d_2 and b_3 in actual graphene by about 50%. As force constants may be varied, for instance, by applying strain, the possibility of finding topological phonon phases in suitably engineered graphene or in other 2-d materials with the honeycomb structure can not be discarded *a priori*.

Discussion The results reported in this letter show that the methods of TQC can be adapted to the search for topologically non-trivial phonons, with the crystal structure as input data. There are, however, some issues that should be addressed. One is the proper definition of fragile topology for phonons. When the irreps of an isolated subset of bands can be obtained as a difference $BR_1 - BR_2$ of band representations, the addition of a trivial band that transforms according to BR_2 ‘trivializes’ the fragile topology [25]. In the case of electrons, the states transforming as BR_2 can, in principle, be found in the crystal, maybe as core orbitals deep in the valence bands, maybe forming high energy conduction bands. Obviously, this is not the case for phonons, where the number of bands is limited to $3N_A$ for a crystal with N_A atoms per primitive cell. Another question is the possible connectivity constraints derived from the existence of acoustic bands. This problem does not arise in graphene, where in- and off-plane modes decouple, but may be an issue with other systems.

Acknowledgments It is a pleasure to thank A. Bernevig, B. Bradlyn, J. Cano and Z. Song for useful discussions and suggestions. This work has been

supported in part by Plan Nacional de Altas Energías Spanish MINECO grant FPA2015-64041-C2-1-P and by Basque Government grant IT979-16.

-
- [1] F. D. M. Haldane, Phys. Rev. Lett. **61**, 2015 (1988).
- [2] C. L. Kane and E. J. Mele, Phys. Rev. Lett. **95**, 226801 (2005).
- [3] C. L. Kane and E. J. Mele, Phys. Rev. Lett. **95**, 146802 (2005).
- [4] Y.-T. Wang, P.-G. Luan, and S. Zhang, New Journal of Physics **17**, 073031 (2015).
- [5] T. Kariyado and Y. Hatsugai, Scientific Reports **5**, 18107 EP (2015).
- [6] Y. Liu, Y. Xu, S.-C. Zhang, and W. Duan, Phys. Rev. B **96**, 064106 (2017).
- [7] P. Wang, L. Lu, and K. Bertoldi, Phys. Rev. Lett. **115**, 104302 (2015).
- [8] Y. Liu, C.-S. Lian, Y. Li, Y. Xu, and W. Duan, Phys. Rev. Lett. **119**, 255901 (2017).
- [9] B. Bradlyn, L. Elcoro, J. Cano, M. G. Vergniory, Z. Wang, C. Felser, M. I. Aroyo, and B. A. Bernevig, Nature **547**, 298 EP (2017).
- [10] M. G. Vergniory, L. Elcoro, C. Felser, B. A. Bernevig, and Z. Wang, arXiv e-prints (2018), arXiv:1807.10271 [cond-mat.mtrl-sci].
- [11] J. Zak, Phys. Rev. Lett. **45**, 1025 (1980).
- [12] J. Zak, Phys. Rev. B **23**, 2824 (1981).
- [13] J. Cano, B. Bradlyn, Z. Wang, L. Elcoro, M. G. Vergniory, C. Felser, M. I. Aroyo, and B. A. Bernevig, Phys. Rev. B **97**, 035139 (2018).
- [14] The index i runs over all the atomic orbitals or, more generally, Wannier functions in a primitive unit cell.
- [15] C. J. Bradley and A. P. Cracknell, *The Mathematical Theory of Symmetry in Solids* (Clarendon Press, Oxford, 1972).
- [16] L. Michel and J. Zak, Physics Reports **341**, 377 (2001).
- [17] L. Michel, M. B. Walker, and J. Zak, Phys. Rev. Lett. **74**, 4871 (1995).
- [18] M. I. Aroyo, J. M. Perez-Mato, C. Capillas, E. Kroumova, S. Ivantchev, G. Madariaga, A. Kirov, and H. Wondratschek, Zeitschrift für Kristallographie **221**, 15 (2006).
- [19] M. I. Aroyo, A. Kirov, C. Capillas, J. M. Perez-Mato, and H. Wondratschek, Acta Crystallographica Section A **62**, 115 (2006).
- [20] B. Bradlyn, L. Elcoro, M. G. Vergniory, J. Cano, Z. Wang, C. Felser, M. I. Aroyo, and B. A. Bernevig, Phys. Rev. B **97**, 035138 (2018).
- [21] M. G. Vergniory, L. Elcoro, Z. Wang, J. Cano, C. Felser, M. I. Aroyo, B. A. Bernevig, and B. Bradlyn, Phys. Rev. E **96**, 023310 (2017).
- [22] J. Cano, B. Bradlyn, Z. Wang, L. Elcoro, M. G. Vergniory, C. Felser, M. I. Aroyo, and B. A. Bernevig, Phys. Rev. Lett. **120**, 266401 (2018).
- [23] In that sense the two off-plane phonon bands are trivial and will not be further considered in this Letter. Note, however, that they host a Weyl point at the K -point.
- [24] B. Bradlyn, Z. Wang, J. Cano, and B. A. Bernevig, Phys. Rev. B **99**, 045140 (2019).
- [25] H. C. Po, H. Watanabe, and A. Vishwanath, Phys. Rev. Lett. **121**, 126402 (2018).
- [26] A. A. Maradudin and S. H. Vosko, Rev. Mod. Phys. **40**, 1 (1968).
- [27] For the honeycomb lattice it will be convenient to consider i as a double index (a, \mathbf{R}) , where \mathbf{R} and a specify the unit cell and the sublattice $a = A, B$. See details in the SM.
- [28] F. Wilczek and A. Zee, Phys. Rev. Lett. **52**, 2111 (1984).
- [29] A. A. Soluyanov and D. Vanderbilt, Phys. Rev. B **83**, 035108 (2011).
- [30] J. Zak, Phys. Rev. Lett. **48**, 359 (1982).
- [31] J. Zak, Phys. Rev. Lett. **62**, 2747 (1989).
- [32] A. Alexandradinata, Z. Wang, and B. A. Bernevig, Phys. Rev. X **6**, 021008 (2016).
- [33] S. Kivelson, Phys. Rev. B **26**, 4269 (1982).
- [34] N. Marzari and D. Vanderbilt, Phys. Rev. B **56**, 12847 (1997).
- [35] A. Alexandradinata, X. Dai, and B. A. Bernevig, Phys. Rev. B **89**, 155114 (2014).
- [36] Z. Song, Z. Wang, W. Shi, G. Li, C. Fang, and B. A. Bernevig, arXiv e-prints (2018), arXiv:1807.10676 [cond-mat.mes-hall].
- [37] W. A. Benalcazar, B. A. Bernevig, and T. L. Hughes, Science **357**, 61 (2017), arXiv:1611.07987 [cond-mat.str-el].
- [38] W. A. Benalcazar, B. A. Bernevig, and T. L. Hughes, Phys. Rev. B **96**, 245115 (2017).

Supplemental Material for Phonon Topology on the Time-Reversal Symmetric Honeycomb

Juan L. Mañes¹

¹*Departamento de Física de la Materia Condensada, Universidad del País Vasco UPV/EHU*

S1. PARAMETRIZATION OF THE DYNAMICAL MATRIX

The symmetry constraints on the matrix of force constants for the planar honeycomb have been considered in Ref 1. For the sake a completeness and to set the notation we give here a brief summary of the analysis for the in-plane modes that, according to the main text, are the ones that can exhibit nontrivial topology. The harmonic potential energy for the in-plane modes is given by

$$U = \frac{1}{2} \sum_{i,j} \mathbf{r}_i^t U_{ij} \mathbf{r}_j, \quad (\text{S1})$$

where i, j run over all the atoms² in the lattice, $\mathbf{r}_i = (x_i, y_i)$ is the displacement of atom i from equilibrium and $U_{ij} = U_{ji}^t$ is the matrix of force constants between atoms i and j .

Assuming i, j are n th-nearest neighbors, the 2×2 matrix U_{ij} is parametrized by four real coefficients (a_n, b_n, c_n, d_n) . Pick one n th-nearest neighbor j to the atom i and parametrize U_{ij} as

$$U_{ij} = \begin{pmatrix} a_n + b_n & -c_n - d_n \\ -c_n + d_n & a_n - b_n \end{pmatrix}, \quad (\text{S2})$$

where the parameters are real by time reversal symmetry. Then, if $(i'j')$ is another pair of n th-nearest neighbors such that $\mathbf{d}_{i'j'} = V(g)\mathbf{d}_{ij}$, where $V(g)$ is the vector representation for the symmetry operation g that transforms ij into $i'j'$, we will have

$$U_{i'j'} = V(g)U_{ij}V(g)^{-1}. \quad (\text{S3})$$

1	2	3	4	5	6	7
a_1	a_2	a_3	a_4	a_5	a_6	a_7
b_1	b_2	b_3	b_4	b_5	b_6	b_7
—	—	—	c_4	—	—	c_7
—	d_2	—	d_4	—	d_6	d_7

TABLE S1. Non-vanishing coefficients parametrizing the harmonic potential between n th-nearest neighbors for $n = 1, \dots, 7$.

If the number of n th-nearest neighbors is sufficiently large, we may have several subsets of pairs (ij) unrelated by symmetry. In that case we would need more that one set of parameters (a_n, b_n, c_n, d_n) . For the honeycomb lattice this will happen whenever the number of n th-nearest neighbors is greater than 12, which is the number of elements in $6mm$. On the other hand, the number of independent parameters for given n may be less that four.

This happens if the two atoms (i, j) are left invariant (exchanged) by a symmetry element g , since then Eq. (S3) (combined with $U_{ij} = U_{ji}^t$) becomes a constraint. For the honeycomb lattice, one possibility is to have a mirror m_{\parallel} along the link \mathbf{d}_{ij} . Assuming for simplicity that $\mathbf{d}_{12} = d_{12}\hat{\mathbf{x}}$, under the action of m_{\parallel} , $(x_i, y_i) \rightarrow (x_i, -y_i)$ for $i = 1, 2$. This implies $c_n = d_n = 0$. Another possibility is to have a mirror m_{\perp} perpendicular to \mathbf{d}_{ij} through the midpoint of the link. This exchanges the two atoms and reverses the x components of the displacements, which implies $c_n = 0$. The effect of these constraints is summarized in Table S1 for n up to seven. It is important to realize that, in order to impose a constraint, the parallel mirror m_{\parallel} has to pass *through* the two atoms. A mirror plane that is parallel to \mathbf{d}_{ij} but does not go through ij does *not* impose any constraint on U_{ij} ; it merely relates $U_{i'j'}$ to U_{ij} , where $(i'j')$ are the images of (ij) by the mirror plane. Failing to appreciate this point would lead us to set $d_2 = 0$, as in Ref 1.

These are the only possible constraints on the planar honeycomb lattice for $i \neq j$. For $i = j$, the C_{3z} invariance about each atom implies $U_{ii} = a_0\mathbb{1}$. Note, however, that a_0 is not an independent parameter, due to the global translation invariance of the crystal, which implies $\sum_j U_{ij} = 0$. This guarantees that atom i does not experience any force when all the atoms in the crystal are given a uniform displacement $\mathbf{r}_i = \mathbf{t}$ and is behind the existence of acoustic phonon branches. This is a peculiarity of phonon dynamics without analog in electron hamiltonians, where on-site energies are independent parameters. For the planar honeycomb lattice, as a the result of global translation invariance, we have $a_0 = -3a_1 - 6a_2 - 3a_3 - \dots$.

In what follows it will be convenient to make a change of coordinates from linear to circular polarizations

$$\xi = \frac{1}{\sqrt{2}}(x + iy), \quad \bar{\xi} = \frac{1}{\sqrt{2}}(x - iy). \quad (\text{S4})$$

In these coordinates, the matrix U_{ij} can be written

$$U_{ij} = a_n\mathbb{1}_s + b_ns_x + c_ns_y + id_ns_z, \quad (\text{S5})$$

where s_i are Pauli matrices for phonon ‘spin’, with the upper (lower) components giving the amplitude of the right (left) circular polarization.

S2. DYNAMICAL MATRIX WITH THIRD NEAREST NEIGHBOR INTERACTIONS

The basis vectors for the Bravais lattice are given by

$$\mathbf{e}_1 = \hat{\mathbf{x}}, \quad \mathbf{e}_2 = \frac{1}{2}\hat{\mathbf{x}} + \frac{\sqrt{3}}{2}\hat{\mathbf{y}}, \quad (\text{S6})$$

and are shown in Fig. 1 together with their reciprocal lattice vectors \mathbf{g}_i , which satisfy $\mathbf{g}_i \cdot \mathbf{e}_j = 2\pi\delta_{ij}$. Sites on the $A(B)$ sublattice are at positions $\mathbf{R} + \boldsymbol{\delta}_{A(B)}$, where \mathbf{R} denotes a lattice translation and

$$\boldsymbol{\delta}_A = \frac{1}{3}\mathbf{e}_1 + \frac{1}{3}\mathbf{e}_2, \quad \boldsymbol{\delta}_B = \frac{2}{3}\mathbf{e}_1 + \frac{2}{3}\mathbf{e}_2. \quad (\text{S7})$$

Then each atom is specified by a composite label $i \equiv (a, \mathbf{R})$ that gives the unit cell \mathbf{R} and the sublattice

$a = A, B$. The dynamical matrix is obtained as the Fourier transform of the matrix of force constants

$$D_{ab}(\mathbf{k}) = \sum_{\mathbf{R}} U_{a,0;b,\mathbf{R}} e^{i\mathbf{k} \cdot \mathbf{R}}. \quad (\text{S8})$$

Note that the vector indices (x, y) or $(\xi, \bar{\xi})$ are implicit.

The dynamical matrix acts on 4-component vectors

$$v(\mathbf{k})^t = (\xi_A(\mathbf{k}), \bar{\xi}_A(\mathbf{k}), \xi_B(\mathbf{k}), \bar{\xi}_B(\mathbf{k})) \quad (\text{S9})$$

and can be expressed in terms of Kronecker products of Pauli matrices σ_i for the two sublattices, and s_i for phonon ‘spin’. The result, up to third nearest neighbor interactions is given by

$$\begin{aligned} D(\mathbf{k}) = & -3(a_1 + 2a_2 + a_3)\mathbb{1}_4 + a_1 \left[\left(1 + 2\cos\frac{k_x}{2}\cos\frac{\sqrt{3}}{2}k_y \right) \sigma_x \otimes \mathbb{1}_s - 2 \left(\cos\frac{k_x}{2}\sin\frac{\sqrt{3}}{2}k_y \right) \sigma_y \otimes \mathbb{1}_s \right] \\ & + b_1 \left[\left(1 - \cos\frac{k_x}{2}\cos\frac{\sqrt{3}}{2}k_y \right) \sigma_x \otimes s_x + \left(\cos\frac{k_x}{2}\sin\frac{\sqrt{3}}{2}k_y \right) \sigma_y \otimes s_x \right. \\ & \left. - \sqrt{3} \left(\sin\frac{k_x}{2}\cos\frac{\sqrt{3}}{2}k_y \right) \sigma_y \otimes s_y - \sqrt{3} \left(\sin\frac{k_x}{2}\sin\frac{\sqrt{3}}{2}k_y \right) \sigma_x \otimes s_y \right] \\ & + a_2 \left(2\cos k_x + 4\cos\frac{k_x}{2}\cos\frac{\sqrt{3}}{2}k_y \right) \mathbb{1}_4 + d_2 \left(4\sin\frac{k_x}{2}\cos\frac{\sqrt{3}}{2}k_y - 2\sin k_x \right) \sigma_z \otimes s_z \\ & + b_2 \left[2 \left(\cos k_x - \cos\frac{k_x}{2}\cos\frac{\sqrt{3}}{2}k_y \right) \mathbb{1}_\sigma \otimes s_x + 2\sqrt{3} \left(\sin\frac{k_x}{2}\sin\frac{\sqrt{3}}{2}k_y \right) \mathbb{1}_\sigma \otimes s_y \right] \\ & + a_3 \left[\left(2\cos k_x + \cos\sqrt{3}k_y \right) \sigma_x \otimes \mathbb{1}_s - (\sin\sqrt{3}k_y) \sigma_y \otimes \mathbb{1}_s \right] \\ & + b_3 \left[\left(-\cos k_x + \cos\sqrt{3}k_y \right) \sigma_x \otimes s_x - (\sin\sqrt{3}k_y) \sigma_y \otimes s_x + \sqrt{3}(\sin k_x) \sigma_y \otimes s_y \right]. \end{aligned} \quad (\text{S10})$$

If we set $b_1 = b_2 = b_3 = 0$, the dynamical matrix becomes diagonal in ‘spin’ space, i.e., right and left-handed modes decouple from each other. In that case, the edge modes discussed in the main text are helical modes and the gaps in their spectrum disappear. As the b_i bulk couplings are allowed by all the symmetries in the system, this is a sign of fragile topology. In the gapless limit $b_i = 0$, acoustic and optical edge modes have opposite helicities: if the acoustic right moving edge modes have right circular polarization, then then optical right moving edge modes have left circular polarization and vice versa.

It is interesting to note that, if we neglect third nearest neighbor interactions, the dynamical matrix (S10) is closely related to the Kane-Mele hamiltonian³ for spin-

ful p_z orbitals in graphene, with the two phonon circular polarizations playing, to some extent, the role of electron spin. In fact, comparing (S10) with the Kane-Mele hamiltonian shows that the terms proportional to a_1 have the structure of the Dirac hamiltonian, while the term with d_2 coincides with the Haldane spin-orbit coupling in the Kane-Mele model. On the other hand, the functions of (k_x, k_y) in the terms proportional to b_1 are identical to the ones appearing in the Rashba spin-orbit coupling in the Kane-Mele model, although the matrix structures are different. Actually, writing the couplings in real space shows that the Rashba term in the Kane-Mele model differs from the b_1 -term just by a factor of the imaginary unit i . That both terms manage to be time-reversal invariant reflects the fact that electron spin-1/2

and phonon spin-1 transform differently under time reversal. Another consequence of the different transformation properties of electron and phonon spin, this time under space symmetries, is that the Rashba coupling breaks reflection symmetry by the horizontal mirror plane, while the b_1 -term does not. Finally, one last manifestation of the differences between spin-1/2 and spin-1 systems is the absence of Kramers degeneracy in the phonon spectrum, where we find four different frequencies at the time-reversal symmetric M -point, instead of the two doubly degenerate energies of the electron spectrum.

We mentioned in the main text that in-plane displacements transform according to the vector representation, just like (p_x, p_y) orbitals do. As a consequence, the dynamical matrix for in-plane modes has to be closely related to the hamiltonian for spinless (p_x, p_y) -orbitals in graphene. This is actually the case, as the model in Ref 4 coincides with the dynamical matrix (S10) if we take $(a_1, b_1) \sim (t_\sigma \pm t_\pi)$, $d_2 \sim x$, where (t_σ, t_π, x) are the couplings in Ref 4, and set all the other couplings and the on-site term in (S10) to zero.

S3. PHASE DIAGRAM FOR THE PLANAR HONEYCOMB

The dynamical matrix can be diagonalized analytically at the three high symmetry points in the BZ, and irreps can be assigned to the corresponding eigenmodes. The result may be written as

$$\omega^2(\mathbf{k}, D_a) = \omega^2(\mathbf{k}) + \delta\omega^2(\mathbf{k}, D_a), \quad (\text{S11})$$

where D_a denotes an irrep of the little group $G_{\mathbf{k}}$, $\omega^2(\mathbf{k})$ is common to all the bands at the \mathbf{k} -point and $\delta\omega^2(\mathbf{k}, D_a)$ is specific to each irrep. We obtain

$$\begin{aligned} \omega^2(\Gamma) &= 0 \\ \omega^2(K) &= -3(a_1 + 3a_2 + a_3) \\ \omega^2(M) &= -3a_1 - 8a_2 - 3a_3, \end{aligned} \quad (\text{S12})$$

while $\delta\omega^2(\mathbf{k}, D_a)$ is given in Table S2, where the last column shows the C_{2z} -eigenvalues of the normal modes at the C_{2z} -invariant points Γ and M .

As mentioned in the main text, in order to be in a nontrivial phase $\omega(K_3)$ should be higher or lower than $\omega(K_1)$ and $\omega(K_2)$. A look at the frequencies in Table S2 shows that this implies

$$2\sqrt{3}|d_2| > |b_1 + b_3|, \quad (\text{S13})$$

which is Eq. (1) in the main text. A second necessary condition in order to have two disconnected sets of bands is that $\omega(M_1)$ and $\omega(M_2)$ are both higher or lower than $\omega(M_3)$ and $\omega(M_4)$. This is equivalent to

$$|2b_1 + 4b_2| + |2b_1 - 4b_2| < 2|a_1 - 3a_3|. \quad (\text{S14})$$

Irrep	d	$\delta\omega^2$	C_{2z}
Γ_5	2	$-6(a_1 + a_3)$	+1
Γ_6	2	0	-1
K_1	1	$3\sqrt{3}d_2 + 3(b_1 + b_3)$	-
K_2	1	$3\sqrt{3}d_2 - 3(b_1 + b_3)$	-
K_3	2	$-3\sqrt{3}d_2$	-
M_1	1	$a_1 - 3a_3 + 2b_1 - 4b_2$	+1
M_2	1	$a_1 - 3a_3 - 2b_1 + 4b_2$	+1
M_3	1	$-a_1 + 3a_3 - 2b_1 - 4b_2$	-1
M_4	1	$-a_1 + 3a_3 + 2b_1 + 4b_2$	-1

TABLE S2. $\delta\omega^2(\mathbf{k}, D_a)$ for the little group irreps. d is the dimension of the irrep. The last column indicates the C_{2z} -eigenvalues of the normal modes.

For $|b_1| > 2|b_2|$ this reduces to $2|b_1| < |a_1 - 3a_3|$ while, for $|b_1| < 2|b_2|$, Eq. (S14) is equivalent to $4|b_2| < |a_1 - 3a_3|$. The two cases can be combined into

$$|a_1 - 3a_3| > \text{Max}\{2|b_1|, 4|b_2|\}, \quad (\text{S15})$$

which is Eq. (2) in the Main Text. Assuming that Eqs. (S13, S15) are satisfied, Table S4 identifies the non-trivial topological phases.

Phase	Conditions
Ia	$d_2 < 0$ $a_1 < 3a_3$
Ib	$d_2 > 0$ $a_1 < 3a_3$
IIa	$d_2 < 0$ $a_1 > 3a_3$
IIb	$d_2 > 0$ $a_1 > 3a_3$

TABLE S3. Topologically nontrivial phases.

A minimal model that describes qualitatively the topologically nontrivial phases with WL winding number one (Ia and Ib) can be obtained by keeping only the set of parameters (a_1, b_1, d_2) , with $|a_1| > 2|b_1|$ and $2\sqrt{3}|d_2| > |b_1|$, with a_1 negative for stability. Phases IIa and IIb can be obtained by keeping also a_3 , with $|a_1 - 3a_3| > 2|b_1|$ and $3a_3 < a_1$. Note that this last condition requires $3|a_3| > |a_1|$, which is probably unrealistic for an atomic crystal, but may be attainable for mechanical systems or metamaterials⁶.

A. Locating graphene in the phase diagram

Here we will try to place graphene in the phase diagram for the in-plane phonon system of the planar honeycomb. To this end, we will fit the DFT phonon spectrum reported in Ref 7 to the one obtained from the third-nearest neighbor dynamical matrix (S10).

Table S4 compares the phonon frequencies at the high symmetry points computed by DFT in Ref 7 with the ones obtained by diagonalizing the third-nearest neighbor dynamical matrix (S10) for the following set of pa-

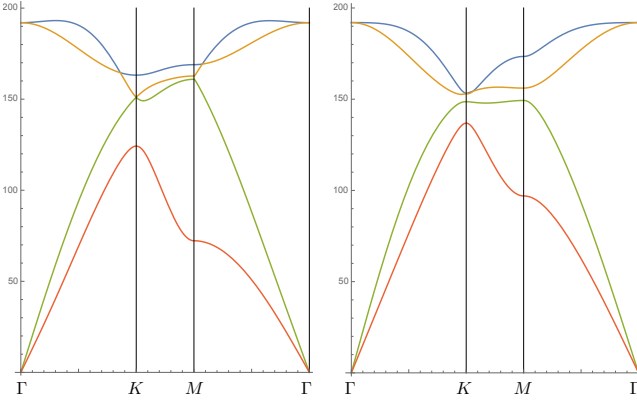


FIG. S1. In-plane phonon spectrum for graphene, obtained by diagonalization of the third-nearest neighbor dynamical matrix. Left: Phonon bands for the values of the parameters that give the best fit to the DFT bands. Right: Phonon bands after increasing d_2 by 70%, while decreasing b_1 and b_3 in the same proportion.

	DFT	3NN
$\omega(\Gamma_5)$	192	192
$\omega(K_1)$	122	124
$\omega(K_2)$	161	163
$\omega(K_3)$	149	151
$\omega(M_1)$	163	161
$\omega(M_2)$	171	169
$\omega(M_3)$	77	72
$\omega(M_4)$	165	163

TABLE S4. Phonon energies in *meV* at the high symmetry points.

rameters, in units of $(\text{meV})^2$

$$\begin{aligned}
 a_1 &= -6.03 \cdot 10^3 & b_2 &= 1.16 \cdot 10^3 \\
 a_2 &= -0.387 \cdot 10^3 & b_3 &= 1.12 \cdot 10^3 \\
 a_3 &= -0.114 \cdot 10^3 & d_2 &= -0.171 \cdot 10^3 \\
 b_1 &= -2.99 \cdot 10^3.
 \end{aligned} \tag{S16}$$

The parameters have been obtained by using the explicit formulae in Table S2 to fit the in-plane bands in Fig. 2 of Ref 7 at the high symmetry points. As these are not labeled by irreps, some trial and error is necessary before the fit can be completed. The goal is to get the best possible agreement at the high symmetry points, while maintaining the overall qualitative features of the spectrum. As shown in Table S4, the energies at the high symmetry points agree within a few percent, and the spectrum in Fig. S1 (left) closely resembles the one in Ref 7.

All the in-plane bands in graphene are interconnected and the spectrum is topologically trivial. But now that we have parametrized the spectrum as in (S16), we can try to see how far graphene is from becoming topological. Plugging (S16) into (S13) yields

$$2\sqrt{3}|d_2| \simeq 0.31|b_1 + b_3|, \tag{S17}$$

while for (S15) the result is

$$\begin{aligned}
 |a_1 - 3a_3| &\simeq 0.95 \cdot 2|b_1| \\
 |a_1 - 3a_3| &\simeq 1.22 \cdot 4|b_2|.
 \end{aligned} \tag{S18}$$

Thus we see that, although inequality (S15) is on the verge of being satisfied, we are further from satisfying (S13), although the couplings are at least the correct order of magnitude.

How much do we need to vary the parameters to get into a topologically non-trivial phase? Assume that we increase the strength of d_2 in the same proportion that we decrease b_1 and b_3 , i.e., we take $d_2 \rightarrow (1+x)d_2$, together with $b_2 \rightarrow (1-x)b_1$ and $b_3 \rightarrow (1-x)b_3$. Then we see that the required inequalities are satisfied for $x \gtrsim .52$. In other words, graphene can enter a topologically nontrivial phonon phase if some couplings are changed by about 50%. Fig. S1(right) shows the in-plane phonon spectrum for $x = 0.7$. As the frequency of $\omega(K_3)$ is greater than $\omega(K_1)$ and $\omega(K_2)$, we are in Phase Ia. Note that phases IIa and IIb are clearly out of reach, as they would require increasing the strength of a_3 by a factor of twenty, from $|a_3| \simeq 0.11 \cdot 10^3$ to more than $|a_1|/3 = 2 \cdot 10^3$.

S4. WILSON LOOP WINDINGS

A. C_{2z} -eigenvalues and WL winding

We mention in the main text that the winding of the WLs can be understood in terms of the C_{2z} -eigenvalues of the normal modes at the two C_{2z} -invariant points Γ and M . Here we fill in the details of the argument following the ideas in Ref 8 and taking into account that, for the in-plane modes of the honeycomb lattice, C_{2z} plays the role of inversion symmetry. The \mathbf{g}_1 -directed WL is defined in the main text by

$$W(k_2) \equiv P e^{i \int_0^{2\pi} dk_1 A_1(k_1, k_2)}, \tag{S19}$$

For fixed k_2 , this formula can be interpreted as the WL for a 1-dimensional system with reciprocal primitive cell $k_1 \in [0, 2\pi]$ along \mathbf{g}_1 . Then, for values of k_2 such that the 1-dimensional system is C_{2z} -invariant, i.e., for $k_2 = 0, \pi$, the number $N_{(-1)}$ of -1 eigenvalues of the WL is given by Eq. (1) in Ref 8, namely

$$N_{(-1)} = |n_{(-)}(0) - n_{(-)}(\pi)|, \tag{S20}$$

where $n_{(-)}(0)$ and $n_{(-)}(\pi)$ are the numbers of normal modes with C_{2z} eigenvalue equal to -1 at $k_1 = 0$ and $k_1 = \pi$ respectively. Now, as Fig. S2 shows, for $k_2 = 0$ the 1-dimensional WL goes through Γ and M'' , and we have

$$N_{(-1)}(k_2 = 0) = |n_{(-)}(\Gamma) - n_{(-)}(M'')|. \tag{S21}$$

This is equal to 2 for phases Ia and Ib, where we have two modes with C_{2z} -eigenvalues η at Γ and $-\eta$ at M , and to 0

for phases IIa and IIb, where the eigenvalues are equal to η at Γ and M . Note that M'' and M are related by a unitary C_{3z} -rotation that does not change the C_{2z} spectrum. As the WL eigenvalues are equal to $e^{2\pi i x(k_2)}$, where $x(k_2)$ is the hybrid Wannier function center, this implies $x(\Gamma) = 1/2$ for phases Ia and Ib and $x(\Gamma) = 0$ for phases IIa and IIb. This is exactly what is observed in Fig. 2 of the main text. On the other hand, for $k_2 = \pi$ the 1-dimensional WL goes through M and M' , and we have

$$N_{(-)}(k_2 = \pi) = |n_{(-)}(M) - n_{(-)}(M')| = 0, \quad (\text{S22})$$

irrespective of the topological phase. Thus $x(M) = 0$ for all the topological phases, in agreement with Fig. 2. For phases IIa and IIb the hybrid Wannier functions sit

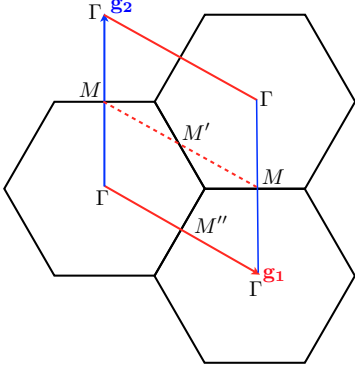


FIG. S2. 1-dimensional Wilson loops for $k_2 = 0$ (red full line) and $k_2 = \pi$ (red dashed line).

at the same point for $k_2 = 0$ and $k_2 = \pi$, and we could have non-winding WLs. This is obviously impossible for phases Ia and Ib, where the WLs necessarily must wind.

B. Crossings at generic points protected by $C_{2z}\mathcal{T}$

Having the same hybrid Wannier centers at $k_2 = 0$ and $k_2 = \pi$ is compatible with non-winding WLs, but also with even winding number. For phases IIa and IIb we find the the WLs have winding number two for all the disconnected branches. As shown in Fig. 2, this involves crossings at generic values of k_2 , and we might worry at their stability against small perturbations. Here we present for phonons the analog of the arguments given in Refs. 5 and 9 for the stability of generic crossings for electrons¹⁰.

The combined operation $C_{2z}\mathcal{T}$ leaves (k_1, k_2) invariant, and the WL loop must satisfy the constraint

$$C_{2z}\mathcal{T}W(k_2)(C_{2z}\mathcal{T})^{-1} = W(k_2). \quad (\text{S23})$$

Writing the unitary operator $W(k_2)$ in terms of the ‘Wan-

nier hamiltonian’ H_W

$$W(k_2) = e^{iH_W(k_2)}, \quad (\text{S24})$$

the constraint becomes

$$C_{2z}\mathcal{T}H_W(k_2)(C_{2z}\mathcal{T})^{-1} = -H_W(k_2), \quad (\text{S25})$$

where the extra minus sign is due to the fact that $C_{2z}\mathcal{T}$ is an antiunitary operation

$$C_{2z}\mathcal{T} = UK, \quad (\text{S26})$$

where U is a unitary matrix and K denotes complex conjugation. In order to determine the form of the matrix U , we note that for generic k_2 the WL is invariant under the magnetic group $2'$ that has only two elements, $2' = \{E, C_{2z}\mathcal{T}\}$, where E is the identity operation. Now, according to Ref 11, the only single-valued irreducible corepresentation for the group $2'$ is 1-dimensional, with the unitary matrix for $C_{2z}\mathcal{T}$ given by $D(C_{2z}\mathcal{T}) = \pm 1$. The two signs give unitarily equivalent corepresentations, and we may take the $+$ sign without loss of generality. As we are considering two-band WLs, these must transform as the 2-dimensional corepresentation obtained by taking two copies of the 1-dimensional irreducible corepresentation. This means that $U = \mathbb{1}_2$ and Eq. (S25) reduces to

$$\mathcal{K}H_W(k_2)\mathcal{K} = H_W(k_2)^* = -H_W(k_2). \quad (\text{S27})$$

Writing H_W as a linear combination of Pauli matrices

$$H_W(k_2) = a_0(k_2)\mathbb{1}_2 + a_x(k_2)\sigma_x + a_y(k_2)\sigma_y + a_z(k_2)\sigma_z, \quad (\text{S28})$$

we see that the constraint (S27) implies

$$H_W(k_2) = a(k_2)\sigma_z. \quad (\text{S29})$$

Had we taken two copies of the 1-dimensional irreducible representation with different signs for $D(C_{2z})$, the constraint would read

$$\sigma_z H_W(k_2)^* \sigma_z = -H_W(k_2), \quad (\text{S30})$$

with solution

$$H_W(k_2) = a(k_2)\sigma_x, \quad (\text{S31})$$

that is related to (S29) by a unitary transformation. In any case, due the periodicity of the Wannier hamiltonian eigenvalues, there will be a crossing whenever $a(k_2) = n\pi$, and this may happen for generic values of k_2 . As we can not add another Pauli matrix, small perturbations will merely shift the position of the crossings, but will not be able to remove them. Note that $a(k_2) = n\pi$ corresponds to $x(k_2) = n/2$, i.e., the protected crossings will take place for $x = 0, 1/2$. Thus the generic crossings at $x = 1/2$ in Fig 2 are protected by $C_{2z}\mathcal{T}$ and the winding of the WL is the winding of the function $a(k_2)$.

-
- ¹ L. Falkovsky, Physics Letters A **372**, 5189 (2008).
- ² For the honeycomb lattice it will be convenient to consider i as a double index (a, \mathbf{R}) , where \mathbf{R} and a specify the unit cell and the sublattice $a = A, B$. See details in the next section.
- ³ C. L. Kane and E. J. Mele, Phys. Rev. Lett. **95**, 146802 (2005).
- ⁴ J. Cano, B. Bradlyn, Z. Wang, L. Elcoro, M. G. Vergniory, C. Felser, M. I. Aroyo, and B. A. Bernevig, Phys. Rev. Lett. **120**, 266401 (2018).
- ⁵ B. Bradlyn, Z. Wang, J. Cano, and B. A. Bernevig, Phys. Rev. B **99**, 045140 (2019).
- ⁶ M. Maldovan, Nature **503**, 209 EP (2013).
- ⁷ F. D. Natterer, Y. Zhao, J. Wyrick, Y.-H. Chan, W.-Y. Ruan, M.-Y. Chou, K. Watanabe, T. Taniguchi, N. B. Zhitenev, and J. A. Stroscio, Phys. Rev. Lett. **114**, 245502 (2015).
- ⁸ A. Alexandradinata, X. Dai, and B. A. Bernevig, Phys. Rev. B **89**, 155114 (2014).
- ⁹ Z. Song, Z. Wang, W. Shi, G. Li, C. Fang, and B. A. Bernevig, arXiv e-prints (2018), arXiv:1807.10676 [cond-mat.mes-hall].
- ¹⁰ For spin-1/2 systems $C_{2z}^2 = \mathcal{T}^2 = -1$, whereas for bosons we have $C_{2z}^2 = \mathcal{T}^2 = 1$.
- ¹¹ C. J. Bradley and A. P. Cracknell, *The Mathematical Theory of Symmetry in Solids* (Clarendon Press, Oxford, 1972).